Physiological Motion Compensation for Neuroscience Research based on Electrical Bio-Impedance Sensing

Yao Zhang, *Student Member, IEEE*, Eric Verschooten, Mouloud Ourak, Kaat Van Assche, Gianni Borghesan, Di Wu, *Member, IEEE*, Kenan Niu, *Member, IEEE*, Philip X. Joris and Emmanuel Vander Poorten, *Member, IEEE*

***Abstract*— Researchers have developed a large number of methods to study the brain's function. One of the most effective techniques is *in vivo* whole-cell patch clamp recording which allows the recording of intracellular neuronal activity. A major issue that drastically reduces the efficiency of *in vivo* patch clamping is the excessive movement of the brain primarily caused by heartbeat and breathing, which can be larger than the size of the neurons under investigation. Motion compensation techniques are complicated due to the lack of sensors to reliably measure local physiologically-induced motion. This work proposes the use of Electrical Bio-impedance (EBI) to the existing patch electrodes in the patching pipette as a proximity sensor. The study further develops an Extended Kalman Filter (EKF) to estimate overall motion and then establishes a motion compensation algorithm for the patch pipette. The proposed method was developed on a custom lab benchtop setup and validated during actual *in vivo* experiments. The results of the lab experiments show a real-time compensatory performance exceeding 80%. The *in vivo* experiments achieved a performance of over 75%, confirming the ability to compensate for real physiologically induced motion. Moreover, the method demonstrated dynamic continuous motion compensation while the electrode was advanced to a neuron, contacting the neuron membrane without damage illustrating the ability to improve neuronal patch clamping. As far as the authors are aware this is the first time that physiologically induced motion can be compensated for this application and this solely relies on EBI.**

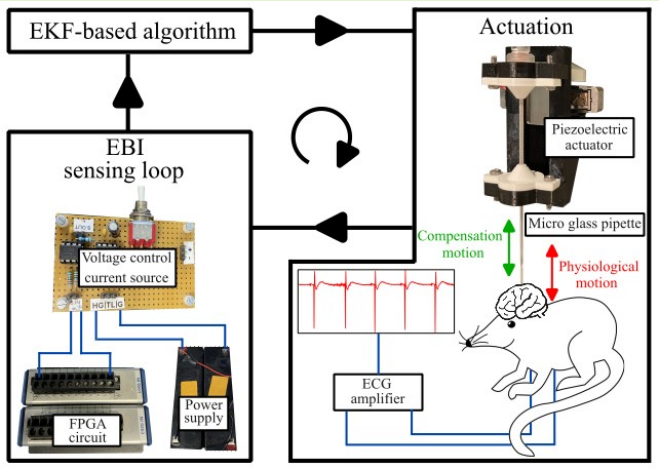

***Index Terms*— Electrical bio-impedance sensing, motion compensation, extended Kalman filter, piezoelectric actuator**

I. Introduction

PROFOUND knowledge of brain function at the cellular level is important for understanding sensory systems [1] and other higher brain functions. It is also important for the development of medicines for neurological disorders such as Parkinson's and Alzheimer's disease [2]. The brain processes a large amount of information through billions of interconnected neurons. To understand neural processing, it is necessary to electrophysiologically measure the internal activity of individual neurons in their natural environment. This requires techniques that allow *in vivo* intracellular recordings [3]. Patch clamp is originally an *in vitro* technique developed in the late 1970s that allows simultaneous recording of neuronal input and output signals with excellent temporal and spatial resolution [4]. Since the 2000s, this technique has been adopted for *in vivo* measurements in living organisms [5]. During the whole-cell patch clamping procedure, a glass micropipette filled with conductive solution is inserted into the brain and advanced to a neuron of interest. Then, the pipette is brought into contact with the neuronal membrane after which it is locally aspirated to make electrical internal contact [6], called a "patch". However, making an *in vivo* patch is a huge

This project has received funding from an internal KU Leuven C3 project 3E200471 and a grant from the Belgian FWO [SB/1S96922N]. (*Corresponding author: Yao Zhang*)

Yao Zhang, Mouloud Ourak, Kaat Van Assche, Di Wu, and Emmanuel Vander Poorten are with the Department of Mechanical Engineering, KU Leuven, Belgium (e-mail: yao.zhang@kuleuven.be).

Eric Verschooten and Philip X. Joris are with the Laboratory of Auditory Neurophysiology, Neurosciences, KU Leuven, Belgium.

Gianni Borghesan is with the Department of Mechanical Engineering, KU Leuven, Belgium, and also with Flanders Make, Belgium.

Kenan Niu is with the Faculty of Electrical Engineering, University of Twente, Netherlands.

challenge with limited success due to the small size of neurons ($\sim$ 10 µm) [7], the lack of visualization [8], and especially the inherent physiologically induced motion by heartbeat and breathing [9]. The latter involves the risk of an uncontrolled penetration of the neuron. If this happens the whole procedure needs to be repeated with a new micropipette [10].

Different electrophysiological studies reported various strengths in brain motions. For instance, Lee *et al.* [11] found in anesthetized mice a 10 µm peak-to-peak heartbeat-induced motion at 6 Hz and almost no breathing-induced motion. Fee *et al.* [12] found similar induced motions in rats between 10 - 40 µm for the heartbeat and a 1 µm for breathing. However, they also found the opposite with a stronger induced breathing component between 10 - 30 µm and almost no heartbeat contribution (2 - 4 µm). Gilletti *et al.* [13] also observed (inward) brain motions in rats, but with much larger amplitudes up to even 60 µm. Lateral micromotion of the brain is not dominant in electrophysiological studies. It is less critical than motion in the normal direction and can be in the first instance ignored because the pulled glass microelectrodes for intracellular recording, while axially stiff, are laterally much more compliant [12], [13]. These studies also illustrate that the physiologically induced brain motion can be larger than the actual size of the neuron itself, making patching practically impossible in such circumstances. Another complicating and dynamic factor to consider is the drift of amplitude motion over time. For example, in adult rats, Sharafkhani *et al.* [14] observed amplitude shifts between 10 - 60 µm over a 5-minute period.

Manual patching requires high technical skills and much perseverance, as the success rate of patching a neuron is very low (less than 30%), even in experienced hands [6], [15]. Several attempts have previously been made to improve the delicate high-precision procedure for approaching the neuron. An experimental setup consisting of a motorized manipulator with a gripper holding a glass micro-pipette was designed by Lee *et al.* [16] to make this high-precision required procedure more controllable. The patch clamp procedure was refined by Kodandaramaiah *et al.* [17] with a more advanced platform adding an automatic pressure system to the pipette to perform the actual patch. One of the difficulties of *in vivo* patching is that it is a "blind" procedure. This problem was addressed by the introduction of assisted two-photon microscopy, in which a fluorescence-stained pipette and a tagged neuron are visualized [18]–[20]. This approach was found to facilitate the *in vivo* patch clamp procedure, but has limitations, including depth restriction of $\sim$ 1 mm, a limitation in accessibility and location, and it does not compensate for brain motions.

The latter was addressed by a few studies [12], [15] that physically compensated the pipette for the physiological motion. For instance, Fee *et al.* [12] proposed a mechanical stabilization system based on a linear finite impulse response filter that extracts motion information by using a filtered electrocardiogram (ECG) and respiratory pressure. Stoy *et al.* [15] proposed a similar approach, where the impulse response is computed from both ECG and breathing signal. In these studies, the ECG and respiratory events were used to compensate for motion by an average extracted impulse response of heart rate/breathing, in which a real-time motion estimation was not foreseen and had to be manually scaled in amplitude. In addition to neuroscience, motion compensation is also attracting the attention of different medical applications with various approaches, such as imaging-assisted techniques [21]–[23], novel sensory feedback [24], [25], and machine/deep learning methods [26]–[28].

To overcome the imperfections of previous motion compensation methods, a novel method based on an Extended Kalman Filter (EKF) and Electrical Bio-impedance (EBI) sensing is proposed in this work. EBI is a recently developed impedance-based non-invasive technique for quantifying the composition of biological tissue [29]–[31]. It is used in various applications, such as in eye surgery for puncture detection [32] and proximity sensing [33], abnormal tissue detection and measurement in the prostate [34], the neck [35], lymph nodes [36], and muscle contraction [37]. The sensing principle of EBI is highly compatible with the kind of micro-pipettes used for patch clamping [15] and is therefore used in this study as a proximity detector to observe the motion of a structure at the front of the pipette. To the authors' knowledge, this is the first time that a control strategy for physiological motion compensation has been presented that utilizes EKF estimation with EBI feedback.

The main contributions of this work are:

- creation of a motion controller architecture based on EKF estimation and EBI proximity detection.
- development of two dedicated mechanical setups: a benchtop test setup and *in vivo* setup.
- validation of the proposed algorithm using the benchtop setup and synthetical heartbeat/breathing motion,
- determination of *in vivo* feasibility in animal experiments and further verification of control strategy.

The remainder of the paper is organized as follows: Section II introduces the proposed motion compensation discussing the physiologically induced motion, EBI sensing, EKF approach with two different observation models, and the control strategy. Section III covers the benchtop setup and verifies the two proposed observational models on the generated synthetic motion. Section IV covers the *in vivo* setup and validates the motion controller. Section V discusses the results and section VI draws the conclusions.

II. EBI-based Motion Compensation

A. Physiological Induced Motion

The first step undertaken was to link the brain motion to its physiological origin in anesthetized animals. For this purpose, vibrometry was performed on the cerebellar surface (Ethical approval number: P071/2022) of Mongolian Gerbils using a chromatic confocal sensor (CCI; STIL® O3PS0382002; sample frequency: 70 kHz; resolution: 70 nm). The result of a typical surface measurement is shown in Fig. 1(a) which exhibits a superposition of two different periodic components: a fast alternating component with a period of approximately 0.38s corresponding to the heartbeat, and a breathing component with larger perturbations lasting four times as long. The

induced amplitudes of heartbeat and breathing are approximately 10 µm and 8 µm, respectively, and are consistent with previous observations in literature (see also Sec. I).

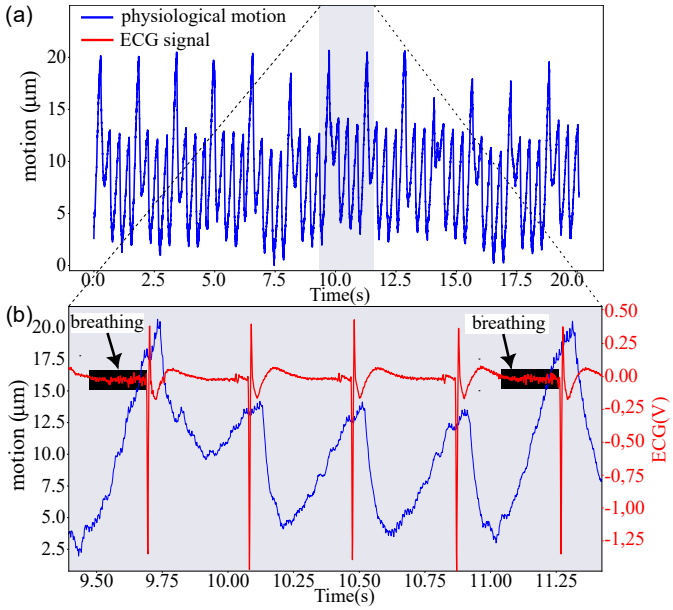

Fig. 1. (a) *In vivo* physiological motion. (b) Zoomed portion of physiological motion signal (in blue) with superpositioned ECG signal (in red).

Figure 1(b) shows an enlarged time slice of Fig. 1(a) covering one breathing period which equals four heartbeat periods (blue trace). The figure also includes an overlay of the animal's electrocardiogram (ECG; red trace). The signal was obtained below the armpits, across the chest with a low noise differential amplifier (SRS® SR560; band-pass filter: 0.1 - 2 kHz). The ECG visually confirms that the two previously mentioned components are indeed of physiological origin. This is evident by the strong correlation 1) between the QRS complexes (rapid negative-positive-negative alternations) in the ECG and positive crests in the motion; and 2) between the muscle breathing artifacts in the ECG (see two black rectangles), and the two largest positive motion crests at approximately 9.75 and 11.25 s. Note that the large crests are in fact superpositions of both physiological components.

B. EBI for Neuroscience Research

Due to specific limitations of the brain, such as the small size of neurons (∼10 µm), lack of external space, the limited penetration depth of photons, and the anatomical complexity of the brain itself, it is practically impossible to optically measure the motion of neurons deeper inside the brain. As a good alternative, an EBI approach is applied in which the (patch) micro-pipette is enabled as a proximity sensor. The underlying principle is that the distance to an object (e.g., a neuron) is estimated by the electrical impedance at the front of the pipette. The fully implemented version of our custom EBI is able to measure the complex impedance (resistance and reactance) over a large frequency range, but because it is deployed as a motion sensor we use only the most relevant impedance at the lowest available frequency (here 156.25 Hz).

Figure 2(a) shows the lumped model of the principle electrical circuit, which consists of an input source (V_{input}), a voltage-controlled current source (VCCS), and a glass micropipette. The components $R_{pipette}$ and $C_{pipette}$ represent the complex impedance of the glass pipette. R_{var} is the resistance of the path between the opening at the front of the glass pipette and the external medium (normally cerebrospinal fluid). Its value depends on the proximity of an object (e.g., a moving neuron) and is approximately inversely proportional to the distance d between the pipette tip and the closest object. For motion compensation, R_{var}, and more specifically its variation is important here, which cannot be measured directly and independently. Nevertheless, the variation of the total impedance (AC component) forms a good approximation at low frequencies where $C_{pipette}$ is neglectable. The total impedance is the ratio of the induced voltage (V_{output}) to the current $I_{pipette}$ imposed by the VCSS, where $I_{pipette}$ is equal to the input voltage (V_{input}) times the VCCS's transconductance (g_m). V_{input} is generated by a Field-Programmable Gate Array (FPGA, CompactRIO, National Instruments®) circuit, which also performs the complex impedance calculations in real time. To filter out high-frequency noise at the output of the pipette, a first-order lowpass IIR filter is implemented in the FPGA circuit. The input signal is a periodic signal consisting of a series of spectral components with power 2 between 156.25 Hz and 20 kHz (i.e., 156.25, 312.5, 625, ..., 20000 Hz), such that the periods are an integer multiple of the length of the (inverse) Fourier transform (n=128; SR= 20 kHz), preventing spectral leakage. As mentioned earlier, only the lowest frequency is used for impedance in this study.

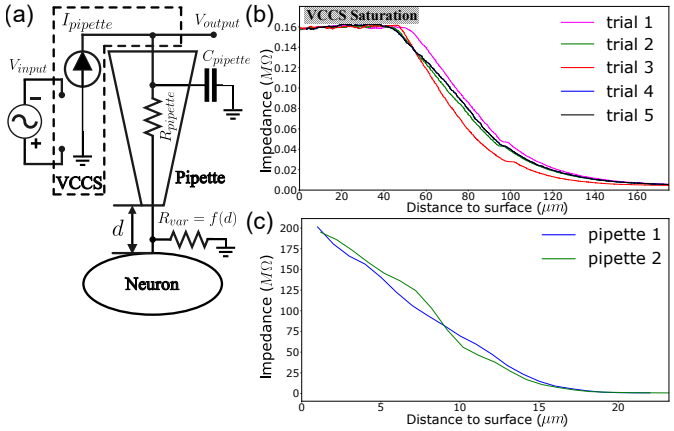

Fig. 2. (a) Equivalent electrical diagram. (b) Example of repeated benchtop setup impedance-distance relationships between using an un-pulled pipette and Parafilm®. (c) Example of repeated impedance-distance relationships on the *in vivo* setup with two pulled pipettes.

Figure 2(b) shows an example of repeated (n=5) measured impedance-distance relationships on the benchtop setup (see III-A) between an un-pulled glass pipette and Parafilm® surface immersed in conductive saline, here simulating a neuron in the brain. Figure 2(c) shows the relationships for two pulled glass pipettes as used in the in vivo experiments, measured under similar conditions. Besides the VCCS saturation region, the general trend of the gradient is decreasing monotonically where it is inversely proportional at long distances and satu-

rating at close distances. When the tip of the pipette is close to the Parafilm®, the electrical impedance and thus V_{output} will dramatically increase until VCCS saturation is reached. The un-pulled glass pipettes have $R_{pipette}$ and $C_{pipette}$ values of about 5 $k\Omega$ range and 1 pF, respectively (1B100F-6, World Precision Instruments®, USA); the pulled pipettes have a typical $R_{pipette}$ between 5 $k\Omega$ and 1 $M\Omega$. The final impedance values also depend on the concentration of electrolyte solution used in the pipette. For *in vivo* patch clamp experiments pulled micro-pipettes are used with a much finer tip and larger impedance values ($R_{pipette}$: 0.5 $M\Omega$ - 2 $M\Omega$; $C_{pipette}$: > 1 pF). In that case, an intracellular amplifier is used with built-in nA VCCS and pipette impedance compensation. Pipette compensation is recommended but not necessary to perform motion compensation.

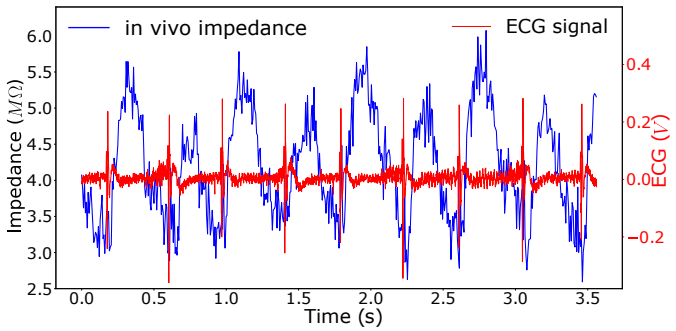

Fig. 3. Example of an *in vivo* impedance measurement with a pulled pipette, together with the corresponding ECG.

Figure 3 shows a typical example of an *in vivo* impedance measurement (blue trace) with a moving neuron. The corresponding ECG signal (red trace), which was obtained in the frontal direction across the chest (the ground electrode connected was connected to the animal's nape of the neck) is included in this measurement. The breathing period is twice that of the heartbeat, as evidenced by the alternating varying size of the crests. Similar to the CCI measurement in Fig. 1(b), there is also here a good correlation between the phase of the impedance and the timing of the QRS profile in the ECG. Note that impedance measurement compared to CCI have a larger amount of noise (mainly unrelated physiological activity), and the polarity is opposite due to the inverse relationship with distance (Fig. 2(b)).

C. Extended Kalman Filter

In vivo motion compensation is not a simple problem that can be solved by simple means such as passive filtering and feedback. There are several challenges, some already mentioned in Section I and Section II-B that all need to be addressed at once. The most critical challenges identified here are: the non-linearity and noise of the EBI sensor, the simultaneous compensation of two superimposed motions, the requirement of strict phase alignment with the periodic motions, and the dynamic nature of the motions themselves. Given these requirements, a dynamic model-based compensation approach, relying on an EKF is adopted. Rather than servoing or compensating motion based on noisy sensor data, the compensation is conducted based on the estimated hidden noiseless model state.

Kalman Filters (KFs) are model-based filters that are often employed to estimate the hidden states of a dynamic system [38]. The basic KF is originally developed for linear systems [39], but later improved to Extended Kalman Filter (EKF) for non-linear systems, such as in this work. The EKF is a Bayesian filter based on the hidden Markov model [40]. The state space model of the EKF is expressed as:

$$\hat{\boldsymbol{x}}(t+\Delta t) = \boldsymbol{F}(\Delta t)\hat{\boldsymbol{x}}(t) + \boldsymbol{\mu}(t) \tag{1}$$

$$z(t) = h(\hat{\boldsymbol{x}}(t)) + v(t) \tag{2}$$

The vector $\hat{\boldsymbol{x}}(t)$ is a vector that collects estimates of the states at current time t. Whereas $\hat{\boldsymbol{x}}(t+\Delta t)$ is the prediction of the states at next time step, with Δt is the time step. $z(t)$ is the input signal which is provided by the EBI. $\boldsymbol{F}(\Delta t)$ is the state transition matrix and $h(\hat{\boldsymbol{x}}(t))$ is the system's observation model. Here, all states are assumed to evolve through a random walk, with $\boldsymbol{\mu(t)} \sim \mathcal{N}(\boldsymbol{0}, \boldsymbol{Q})$ the process noise. It is used to describe the deviation between the estimation from the chosen model and the input sensor signal, which include several different noise sources from the environment. The measurement noise of the EBI sensor is $v(t) \sim \mathcal{N}(0, R)$, which is the uncertainty associated with the EBI sensor. The $\boldsymbol{Q_0}$ and R_0 are initial guesses that were estimated from experiences in previous experiments where they were calculated based on the collected data from the EBI sensor. The procedure of the EKF estimation is presented in Algorithm 1. The whole EKF procedure is recursive [41], such that state estimates are updated as soon as new sensor readings arrive. And if there is a missing measurement, the update step will be skipped and keep the last state estimation.

Algorithm 1: Extended Kalman Filter [43]

initialize $\boldsymbol{P_0}, x_0, R_0$ *and* $\boldsymbol{Q_0}$;
while *EBI signal input* **do**
  $\hat{\boldsymbol{x}}_{\boldsymbol{k}}^{-} = \boldsymbol{f}(\hat{\boldsymbol{x}}_{\boldsymbol{k-1}})$; /* Prediction step */
  $\boldsymbol{P}_{\boldsymbol{k}}^{-} = \boldsymbol{F_k P_{k-1} F_k^T} + \boldsymbol{Q_0}$;
  $\boldsymbol{K_k} = \boldsymbol{P_k^- H_k^T}/(\boldsymbol{H_k P_k^- H_k^T} + R_0)$; /* Update step */
  $\hat{\boldsymbol{x}}_{\boldsymbol{k}} = \hat{\boldsymbol{x}}_{\boldsymbol{k}}^{-} + \boldsymbol{K_k}(z_k - h(\hat{\boldsymbol{x}}_{\boldsymbol{k}}^{-}))$;
  $\boldsymbol{P_k} = (\boldsymbol{I} - \boldsymbol{K_k H_k})\boldsymbol{P_k^-}$;
  $\hat{z}_k = h(\hat{\boldsymbol{x}}_{\boldsymbol{k}})$; /* Output step */
  $k \rightarrow k+1$;
end

Legend

$\hat{\boldsymbol{x}}_{\boldsymbol{k}}^{-}$	Prediction of states at time step k
$\boldsymbol{P}_{\boldsymbol{k}}^{-}$	Predicted error covariance matrix
$\boldsymbol{P_k}$	Error covariance matrix
$\boldsymbol{F_k}$	State transition matrix
$\boldsymbol{Q_0}$	Process noise covariance
$\boldsymbol{K_k}$	Kalman gain
$\boldsymbol{H_k}$	Observation matrix
R_0	Measurement noise covariance
z_k	EBI sensor measurement at time k
$\hat{z}_k$	Final predicted output

From the preliminary CCI and EBI measurements in Fig. 1 and Fig. 2, and related works in the literature [11], [12], [22], [42], the physiologically induced motion of heartbeat and breathing can be roughly approximated by a sinusoidal signal. Based on this approximation, two different observation models $h(\hat{\boldsymbol{x}}(t))$ are proposed. A first observation model possessing a single dominant mode that corresponds to the heartbeat (or alternatively breathing) and another with additionally a mode that corresponds to the motion induced by breathing are proposed.

1) Heartbeat-induced motion: For the motion induced by heartbeat only, an observation model $h(\hat{\boldsymbol{x}}(t))$ based on a single

sinusoid is proposed:

$$\begin{aligned} h(\hat{\boldsymbol{x}}(t)) &= c(t) + r_1(t)\sin(\omega_1(t)t + \phi_1(t)), \\ &= c(t) + r_1(t)\sin(\theta_1(t)), \end{aligned} \tag{3}$$

where $c(t)$ is a motion offset, $r_1(t)$ the amplitude, ω_1 the angular frequency, and $\theta_1(t) = \omega_1(t)t + \phi_1(t)$ the (instantaneous angular) phase with $\phi_1(t)$ a phase shift. The state vector is here defined as

$$\hat{\boldsymbol{x}}(t) \triangleq [c(t), r_1(t), \omega_1(t), \theta_1(t)]^T \tag{4}$$

and is estimated with (1). The corresponding state transition matrix is equal to

$$\boldsymbol{F}(\Delta t) = \begin{bmatrix} \boldsymbol{I_{2\times 2}} & 0 & 0 \\ \boldsymbol{0_{1\times 2}} & 1 & 0 \\ \boldsymbol{0_{1\times 2}} & \Delta t & 1 \end{bmatrix}, \tag{5}$$

with diagonal matrix $\boldsymbol{I_{2\times 2}}$ and zero matrix $\boldsymbol{0_{1\times 2}}$. The observation matrix is equal to

$$\begin{aligned} \boldsymbol{H^T}(\Delta t) &= \left(\frac{\partial h}{\partial x}\right)^T \Big|_{\hat{x}(t+\Delta t|t)=F(\Delta t)\hat{x}(t|t)} \\ &= \begin{bmatrix} 1 \\ \sin(\hat{\theta}_1(t+\Delta t \mid t)) \\ 0 \\ \hat{r}_1(\Delta t \mid t)\cos(\hat{\theta}_1(t+\Delta t \mid t)) \end{bmatrix}, \end{aligned} \tag{6}$$

with $\hat{x}(t+\Delta t \mid t)$ the estimated states of the next time step.

2) Heartbeat and breathing-induced motion: For the combined heartbeat and breathing-induced motion, an observational model $h(\hat{\boldsymbol{x}}(t))$ based on the superposition of two sinusoids is proposed:

$$h(\hat{\boldsymbol{x}}(t)) = c(t) + r_1(t)\sin(\theta_1(t)) + r_2(t)\sin(\theta_2(t)). \tag{7}$$

The chosen state vector is equal to

$$\hat{\boldsymbol{x}}(t) \triangleq [c(t), r_1(t), r_2(t), \omega_1(t), \theta_1(t), \omega_2(t), \theta_2(t)]^T, \tag{8}$$

where $r_1(t), \omega_1(t), \theta_1(t)$ and $r_2(t), \omega_2(t), \theta_2(t)$ represent the amplitude, angular frequency, and phase for heartbeat and breathing, respectively. Based on the state vector (8), the state transition matrix and the observation matrix become

$$\boldsymbol{F}(\Delta t) = \begin{bmatrix} \boldsymbol{I_{3\times 3}} & \boldsymbol{0_{3\times 1}} & \boldsymbol{0_{3\times 1}} & \boldsymbol{0_{3\times 1}} & \boldsymbol{0_{3\times 1}} \\ \boldsymbol{0_{1\times 3}} & 1 & 0 & 0 & 0 \\ \boldsymbol{0_{1\times 3}} & \Delta t & 1 & 0 & 0 \\ \boldsymbol{0_{1\times 3}} & 0 & 0 & 1 & 0 \\ \boldsymbol{0_{1\times 3}} & 0 & 0 & \Delta t & 1 \end{bmatrix}, \tag{9}$$

$$H^T(\Delta t) = \begin{bmatrix} 1 \\ \sin(\hat{\theta}_1(t+\Delta t \mid t))) \\ \sin(\hat{\theta}_2(t+\Delta t \mid t))) \\ 0 \\ \hat{r}_1(\Delta t \mid t)\cos(\hat{\theta}_2(t+\Delta t \mid t))) \\ 0 \\ \hat{r}_2(\Delta t \mid t)\cos(\hat{\theta}_2(t+\Delta t \mid t))) \end{bmatrix}. \tag{10}$$

D. Motion Compensation Control Strategy

The proposed control strategy is based on an EKF estimator with an additional accumulator to accommodate the differentiating effect of the EBI. Recall that the EBI represents not the absolute but the relative motion of the object. The block diagram of the controller with EBI and compensation actuator is shown in Fig. 4(a) and includes one input (Z_k), one output ($x_{output,k}$), and three control blocks (i.e., EKF, amplitude adjustment, and motion controller). The first block in the controller is the EKF. It receives input from the EBI and predicts the new estimates for angular frequency(s) ω_k, phase(s) θ_k, and residual input amplitude(s) r_k.

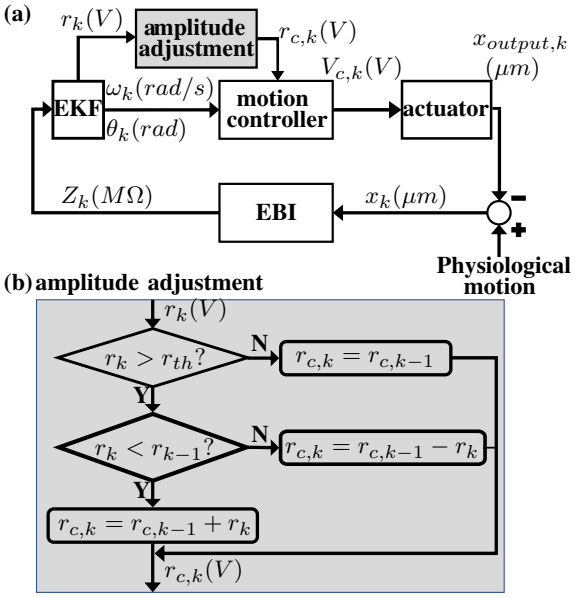

Fig. 4. (a) Control schematic for EBI-based motion compensation. (b) Iterative update of the control voltage amplitude

The second block is the amplitude adjustment block (Fig. 4(b)). It is a dedicated and heuristic block that provides the actual output amplitude(s) $r_{c,k}$. This block is mandatory and copes with the disparity between the absolute motion of the object/pipette and their relative motion sensed by the EBI. The main function is amplitude accumulation and operates as follows: the output amplitude ($r_{c,k}$) is incremented by the EKF-amplitude (r_k) when the EKF-amplitude value is increased; otherwise, it is decremented with r_k. Whenever the EKF amplitude is equal to or less than a preset threshold r_{th}, the previous output amplitude is retained. ω_k and θ_k do not follow this algorithm and are continuously updated by the EKF block to maintain the phase relationship with the residual motion component in the input signal.

The motion controller is the last block in the controller and provides the output control signal ($V_{c,k}$). The output signal provides the instantaneous voltage corresponding to the position of the compensation actuator and is calculated by the observation model ((3) or (7)) and its state vector ((4) or (8)). Note here r_k is substituted by $r_{c,k}$ due to the intermediate amplitude adjustment block.

III. Experiments and Results: Verification

This section verifies the EKF control scheme involving both models proposed in Section II. To assess the performance in a lab setting, a benchtop test setup was developed that was able to generate physiological motions and compensate for them in real time using an EBI input sensor and the proposed EKF model(s). The benchtop setup is explained in the first section and then validated in the remaining two sections.

A. Benchtop Setup

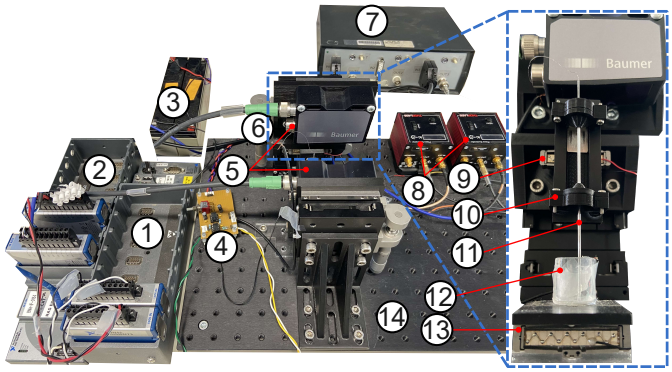

Fig. 5. Benchtop experimental setup: ①–NI® FPGA; ②–NI® EtherCAT; ③–Batteries (+/-12V); ④–VCCS; ⑤–Laser distance sensors; ⑥–3-DoF linear stage; ⑦–Distance sensor power supply; ⑧–Actuator controllers; ⑨–Compensation actuator; ⑩–Pipette holder; ⑪–Pipette; ⑫–Plastic container with Parafilm® on bottom; ⑬–Stimulation actuator; ⑭–Breadboard.

The custom benchtop setup (Fig. 5) contains three main functions: EBI-sensor (①,③,④,⑪), motion generation (②,⑤,⑧,⑬) and motion compensation (②,⑤,⑧,⑨,⑩). All components are directly or indirectly mounted on a rigid aluminum breadboard (⑭) to ensure good mechanical and optical stability. The object under test is a piece of Parafilm® glued to the bottom of a small fluid-filled (physiological saline, 0.9%) plastic container (⑫), which is connected to the ground wire of the EBI sensor. The latter is mounted on a vertically movable platform (⑬), as explained later. The motion generated from ⑬ is transmitted to the plastic container, connecting the Parafilm® and EBI's ground wire, and is sensed by the pipette (⑪) - EBI sensor combination. The main components of this sensor are a National Instrument® FPGA (①) and galvanically isolated VCCS (③,④) that provides the necessary signals/calculus to compute the complex instantaneous impedance (⑪) every 10 ms. For reliability, silver wires are used in the connection of pipette and conductive liquid in the cup.

For motion generation and compensation, high-precision micropositioned piezoelectric actuators (APF503, Thorlabs®, USA) are used (⑨,⑬). The maximum stroke of the actuators is 310 µm and is in range of the typical physiological motion. The pipette is attached to the compensation actuator with a custom braided sleeve pipette holder (⑩) [43]. This assembly is in turn attached to a 3-DoF stage to allow precise manual positioning. The benchtop setup includes two additional high-resolution ($\sim$ 0.7 µm) laser distance sensors (⑤; OM70, Baumer® Group, Switzerland) that measure the actual motion of the pipette and the movable platform at 250 Hz.

The actual motion compensation algorithm is implemented and executed on an external PC. The input (impedance, distance sensors) and output (actuators) signals between the setup and PC were interfaced with a NI® EtherCAT (②) using the open-source robotics middleware suite Robot Operating System (ROS) and ran at 100 Hz.

B. Heartbeat Motion Compensation

According to Sec. II-A and literature, there are mainly two physiological components present in the *in vivo* measurements. In some cases, only one of the two is dominant (mostly heartbeat, and is the focus here) and sufficient to compensate for. Therefore, in this case, a simple sinusoidal stimulation signals $d(t)$ was used according to (11) and sent to ⑬, with f the generation frequency, t time and A the stimulation amplitude, here chosen around 30 µm.

$$d(t) = A\left(\sin\left(2\pi f t\right) + 1\right) \qquad [\mu\text{m}]. \tag{11}$$

To verify the applied control strategy, a range of frequencies (i.e., $f = 1, 2, 3, 4, 5$ Hz) was applied over the full heartbeat range [44]. To validate the repeatability, each measurement was repeated five times. Figure 6 shows one of these results at a frequency of 2 Hz. Panel (a) shows a steady state time fragment of estimated EKF states (i.e., input estimate based on observation model, and accompanying estimated frequency in green) before the actual compensation starts. To evaluate the estimation performance, they are compared to their true counterparts, namely EBI input (red) and generated motion frequency (yellow). Despite the large input noise of the EBI sensor, we confirm by tests and (real) experiments that the internal EKF states of the system are able to accurately and reliably estimate the frequency (green vs. yellow) and more important to estimate the instantaneous target motion (blue vs. red). In this open-loop operation (Fig. 6), it is clear that the EKF acts as a narrow bandpass noise reduction filter, which is the purpose and expected by the imposed model. The dynamic behavior of the compensation algorithm is illustrated in panel (b). It shows the course of the input EBI signal (red), the internal model estimation (blue), and the output voltage (green) when, after stabilizing the internal states (e.g., panel (a)), the compensation output is activated (here at 5 s). After some internal amplitudes adjustments (green steps) and fine-tuning of internal states in the EKF, the input (red) and EKF estimation (blue) are reduced to under-threshold signals. The result of this is shown in panel (c) by the actually measured motions of the pipette (blue; compensation motion), actuator (red; generated motion), and their difference (black; compensation error). Note that the compensation error is due to the internal built-in threshold (see Fig. 4) and to distortions of the actuator that cannot be compensated for, such as harmonics.

To quantitatively evaluate the compensation performance, the error(s) over five periods after the compensation signal has converged were calculated. Three metrics are used, the Root Mean Square Error (RMSE; (12)), the Maximum Absolute

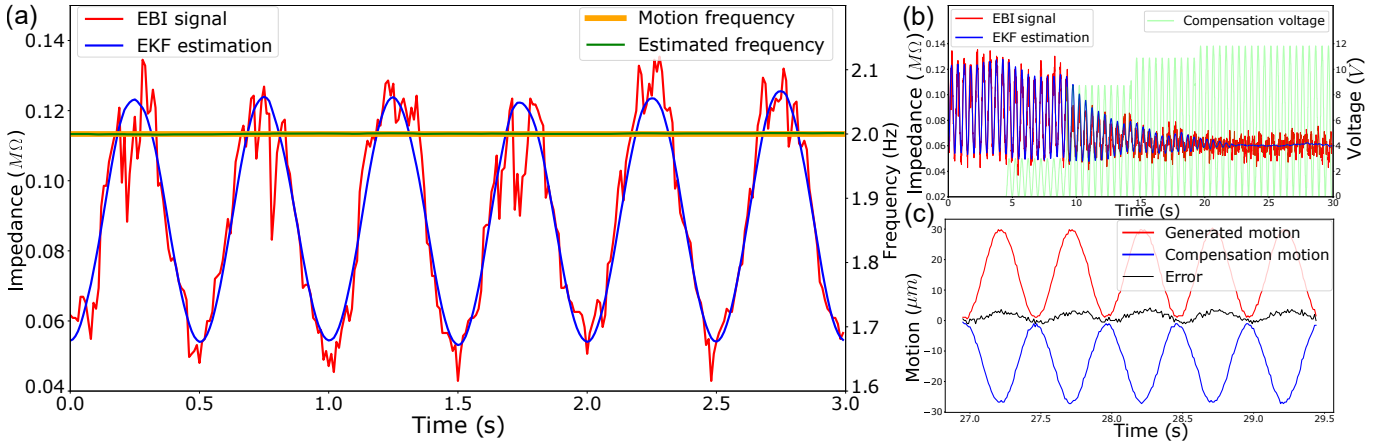

Fig. 6. Fragment of the steady state time at f = 2 Hz. (a) The performance of the EKF on heartbeat motion. (b) Heartbeat motion compensation at 2Hz. (c) Compensation results from laser distance sensors.

TABLE I
RESULTS, OVER 5 GROUPS OF EXPERIMENTS PER FREQUENCY.

Frequency (Hz)	Motion (μm)						Compensation Percentage (%)	
	RMSE		MAE		NRMSE			
	Mean	STD	Mean	STD	Mean	STD	Mean	STD
1	1.75	0.29	4.65	0.57	5.77	1.07	84.82	1.43
2	1.78	0.22	4.54	0.36	6.36	0.17	85.12	1.25
3	2.12	0.31	5.26	0.62	6.81	0.88	83.10	1.73
4	2.10	0.28	5.44	0.54	7.09	0.95	81.71	1.83
5	3.79	0.39	7.81	0.78	12.83	1.82	73.61	2.90

Error (MAE; (13)), and the Normalized Root Mean Square Error (NRMSE; (14)).

$$\text{RMSE} = \sqrt{\frac{\sum_i^N (y_i - \hat{y}_i)^2}{N}}, i = 0, 1, 2, ..., N, \tag{12}$$

$$\text{MAE} = \max\{|y_i - \hat{y}_i|\}, i = 0, 1, 2, ..., N, \tag{13}$$

$$\text{NRMSE} = \frac{\text{RMSE}}{\hat{y}_{\max} - \hat{y}_{\min}} \times 100\%, \tag{14}$$

y_i and $\hat{y}_i$ represent the instantaneous absolute motions of the pipette and stimulation measured by the laser distance sensors. Standard Deviation (STD) is also calculated as the experiments are repeated five times. Additionally, a compensation performance (CP) factor to evaluate how much motion is compensated is introduced:

$$CP = \left(1 - \frac{MAE}{(\hat{y}_i)_{\max} - (\hat{y}_i)_{\min}}\right) \times 100\% \tag{15}$$

Table I summarizes the results for those of the five different frequencies. Across all measurements, the performance factor for the proposed motion compensation algorithm exceeds 80% except for 5 Hz, which is around 74 %. However, it must be noted that this frequency is beyond the physiological range of the Gerbil [44] but is presented here to challenge the proposed controller and setup.

C. Heartbeat and Respiratory Motion Compensation

During *in vivo* patch clamping, one noticed that the induced breathing motion could sometimes not be ignored. Here the more advanced observation model in Sec. II-C.2 is verified. To generate a combined motion of heartbeat and breathing, the following model is used and sent to (13):

$$d(t) = A_1 \left(\sin(2\pi f_1 t) + 1\right) + A_2 \left(\sin(2\pi f_2 t) + 1\right) \quad [\mu\text{m}]. \tag{16}$$

1) Amplitude and frequency: During the *in vivo* patch clamp procedure, the animal is under anesthesia. The breathing and heart rate may increase because the anesthesia level will go down as the experiment progresses [44]. To simulate this behavior in this experiment, the generated motion frequency and amplitudes are made to vary from $A_1 = 25$ μm to 30 μm, $f_1 = 1.9$ Hz to 2.1 Hz, and $A_2 = 8$ μm to 10 μm, $f_2 = 0.8$ Hz to 0.9 Hz with a step change during the motion compensation. Note that the stimulus step changes are not physiological but are introduced to challenge the controller. The results of this test are shown in Fig. 7. Panel (a) shows the EKF responses to a step change of both frequencies and amplitudes. The estimation is able to converge to the ground truth and be back on the right track. Despite the change of amplitude and frequency of the motion causing transient behavior, the amplitude of the EBI still decreases as visible in panel (b). This indicates that the relative motion between the pipette tip and neurons is very well compensated. Panel (c) illustrates the results of one of the five repeated experiments. The black error line fluctuates along with the generated motion but overall with a CP of 81.72%. Table II summarizes the results over the five different groups and shows a small STD for all four valuation metrics.

2) Pipette sudden moving: Another possible scenario that can occur during *in vivo* patch clamping is a sudden change in the position of the pipette due to a sudden movement of the animal, or another (un)intentional perturbation. To relocate the pipette or switch to another neuron, the pipette will need to move forward/away from the neuron. This procedure is basically carried out continuously during the *in vivo* patch clamp experiment. Therefore, this scenario was implemented to test the proposed motion compensation controller. There were in total of five 10 μm step changes (shown in Fig. 8) performed with three approaching steps and two retreating steps. Each step change was made with the micro precision

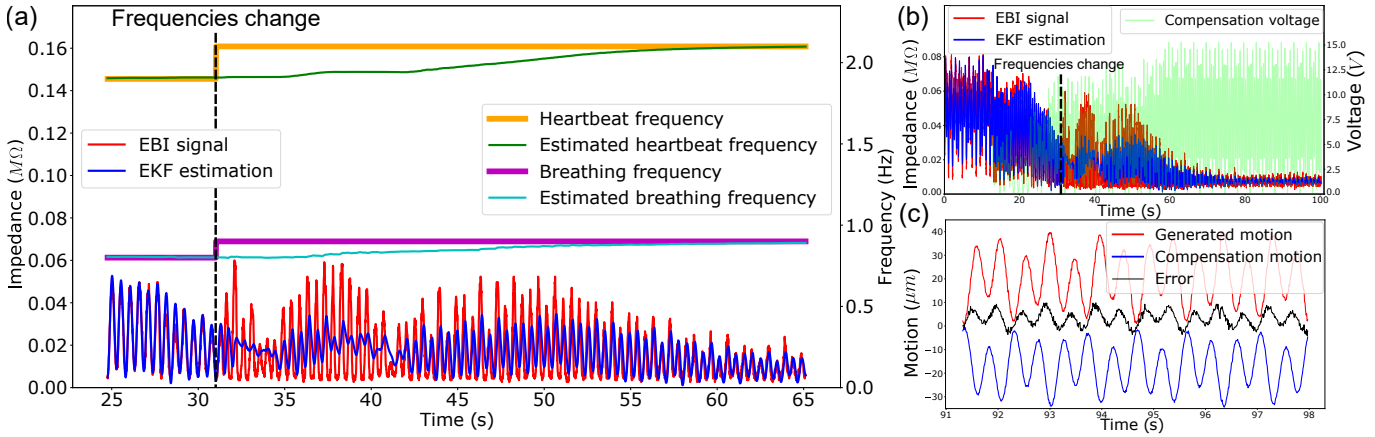

Fig. 7. (a) EKF performance during step changing of frequencies and amplitudes. (b) Compensation with changing amplitude and frequency. (c) Compensation results from laser distance sensors.

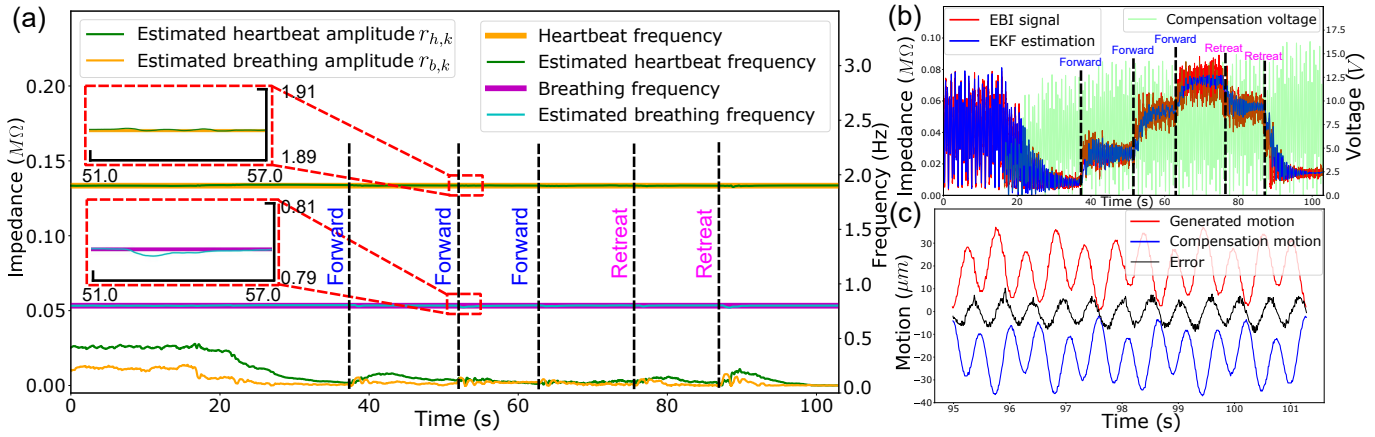

Fig. 8. (a) EKF performance during moving. (b) Compensation during the moving procedure. (c) Compensation results from laser distance sensors.

TABLE II
RESULTS, OVER 5 GROUPS OF CHANGING FREQUENCY EXPERIMENT.

Motion (μm)						Compensation Percentage (%)	
RMSE		MAE		NRMSE			
Mean	STD	Mean	STD	Mean	STD	Mean	STD
3.21	0.38	7.11	0.58	8.25	0.89	81.72	1.28

TABLE III
RESULTS, OVER 5 GROUPS OF PIPETTE MOVING EXPERIMENT.

Motion (μm)						Compensation Percentage (%)	
RMSE		MAE		NRMSE			
Mean	STD	Mean	STD	Mean	STD	Mean	STD
1.86	0.73	4.53	1.18	5.25	2.11	87.23	3.45

linear stage in the setup as shown in Fig. 5. After every forward or retreat, a transient behavior can be observed in the estimated amplitude of heartbeat $r_{h,k}$, breathing $r_{b,k}$, and frequency. However, as is visible in panel (a), the EKF managed to quickly converge to the correct value after each step. Moreover, the estimated amplitudes of both heartbeat and breathing are reduced, and both amplitudes maintain a low level close to zero while step changes happen. In the last step, the pipette is at a different location than before the first step, but it still performs a steady-state compensation as shown in panel (c).

The results of the two different scenarios are listed in Table II and III and show good performance with a CP of more than 80% and an MAE of $\sim$ 7 μm. In principle, this performance is necessary to create a reliable in vivo patch at a neuron with a size of $\sim$ 10 μm [7].

IV. Experiments and Results: In Vivo Validation

After several different scenarios of benchtop verifications, *in vivo* validations in gerbils are performed in this section.

A. In vivo Experimental Setup

The *in vivo* platform (Fig. 9) used in this section was functionally similar to the benchtop with comparable components (see figure caption), but without motion generation and motion measurement components. Other differences specific to the *in vivo* patch clamp procedure were: first, an additional pressure assembly consisting of a flexible silicon pressure tube (⑤), articulating support arm (③), and special pipette adapter (⑨) to provide positive and negative air pressure were added; second, the manual 3-DoF micromanipulator was replaced with a motorized version (SUTTER INSTRUMENT® MP-225, 4-DoF) for remote neuronal search; third, pulled pipettes (⑥) were used with a fine tip (⌀ 2 $\sim$ 3 μm, see inset

Fig. 9 for microscopic view; $Z \sim 1.5\ M\Omega$), whereas for desktop measurements unpulled pipettes ($\varnothing$ 1 mm; $Z \sim 0.1\ M\Omega$) were used; and fourth, a dedicated intracellular patch clamp amplifier (DAGAN® BVC-700A) with internal nA-VCCS and pipette impedance compensation (bridge balance and capacitance compensation) was used.

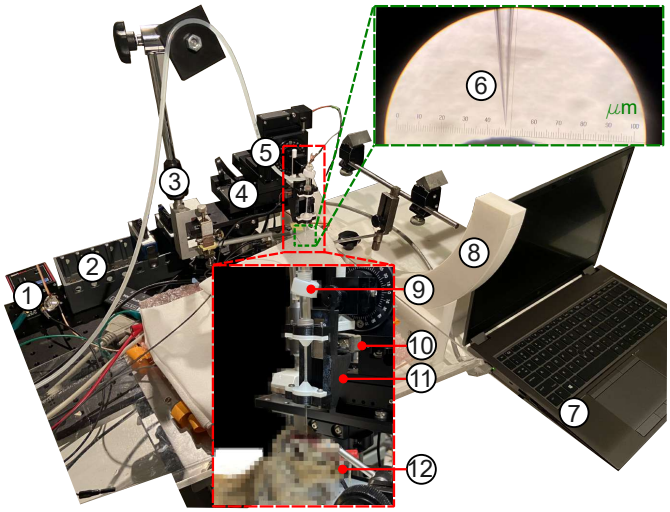

Fig. 9. *In vivo* setup: ①–Piezoelectric controllers; ②–NI® EtherCAT; ③–Articulated clamp; ④–Four-DoF motorized stage; ⑤–Flexible silicon pressure tube; ⑥–Pipette tip; ⑦–Control laptop; ⑧–Animal fixation frame; ⑨–Pipette adapter; ⑩–Piezoelectric actuator; ⑪–Pipette holder; ⑫–Anesthetic gerbils.

The whole assembly was mounted on a small aluminum breadboard in an EM-shielded and soundproof room. The anesthetized animal was mechanically secured with a metal rob to a heavy frame, minimizing additional breathing artifacts. All procedures were approved by the KU Leuven Ethics Committee for Animal Experiments (P071/2022, approved on August 18, 2022) and were in accordance with the National Institutes of Health's Guide for the Care and Use of Laboratory Animals.

B. Stationary Motion Compensation

The *in vivo* procedure, in brief, is as follows. A glass pipette, with silver wire inserted in it as the electrode, under positive pressure is passed through the brain surface and then under reduced pressure advanced to the desired region in the brain. The ground wire of the EBI sensor was placed in the nape of the neck of the animal. Once an object (e.g., a neuron) is detected (increase in impedance), the pressure is further released and the compensation procedure is started. While continuously compensating, the object of interest is approached under the operator's command until contact is made. Finally, negative pressure is applied to the pipette after which the patch is made. During validation, a maximum EBI detection current of 100 nA was applied to minimize the risk of early membrane electroporation, although, if present, it does not affect the validation of the EKF. For comparison with the other EKF signals, the ECG signal was simultaneously monitored and stored.

TABLE IV
RESULTS, OVER 4 GROUPS OF *in vivo* COMPENSATION.

Component	Compensation Percentage (%)	
	Mean	STD
Heartbeat motion	76.05	14.39
Respiratory Motion	75.01	9.44

The *in vivo* performance of the proposed controller is demonstrated in Fig. 10. During stationary motion compensation, the pipette was forwarded toward the neuron of interest until motion was detected by the EBI sensor. The position of the pipette was then fixed and kept at a fixed distance from a neuron. All panels depict the relevant signals (input signal EBI, red; EKF input estimation based on observational model (7), blue; EKF heartbeat and breathing amplitudes estimations, green and yellow; the measured ECG, pink; and the EKF output compensation signal, green) before and after switching on compensation.

A few general observations can be made over the different *in vivo* examples. First, before enabling compensation, the EKF performs good real-time regression (EKF estimation) on real *in vivo* data (EBI). This is shown in more detail by the magnification in Fig. 10(a) 1), which also visualizes the excellent phase correlation between the EBI/EKF estimation and the QRS complex in the ECG. This excellent correlation is also valid for the output (green) as shown in the magnification in Fig. 10(b) 3) after the compensation was started.

A second observation is a sharp reduction in amplitudes of the periodic components in the input signal (EBI) after enabling compensation (Fig. 10(b) 2)). This is indicated by the sudden decrease in the (remaining) estimated heartbeat amplitudes $r_{h,k}$ and breathing amplitudes $r_{b,k}$ at the input and also visually by the EKF estimate.

A third observation is that despite the noisy and rather chaotic input (EBI/EKF estimation before enabling compensation), the output signal (green) appears to be more consistent during effective steady-state compensation.

A problem with *in vivo* experiments is how to quantify performance since the real motions are unknown. As a compromise, one can use the steady states of the input signal (EBI) before and after enabling compensation, which are a good reflection of the un- and compensated motions, respectively. The compensation percentage then becomes

$$CP_{vivo} = \left(1 - \frac{mean(A_{uncompen})}{mean(A_{PP})}\right) \times 100\%, \qquad (17)$$

where $A_{uncompen}$ is the peak-to-peak amplitude of uncompensation leftover EBI and A_{PP} is the peak-to-peak EBI amplitude without motion compensation. Table IV illustrates the results of CP_{vivo} of both components, in which more than 75% motion is compensated and the following approach to neurons procedure can be performed.

C. Dynamic Motion Compensation

This subsection illustrates a further step in the patch process in which compensation is achieved while advancing

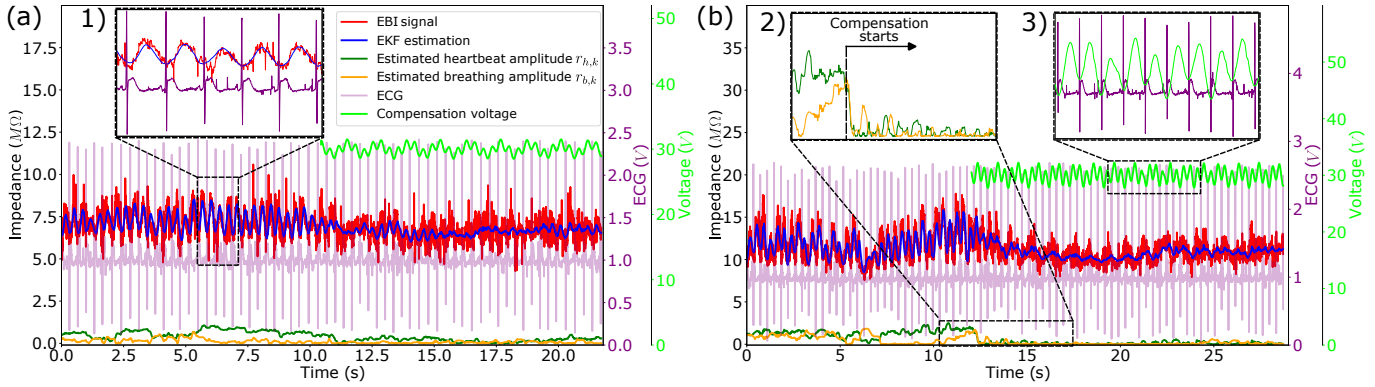

Fig. 10. Two examples ((a) and (b)) of *In vivo* motion compensation at a fixed distance from a moving object (e.g., neuron). 1) The EKF estimation along with the ECG. 2) Decrease of estimated amplitudes of heartbeat $r_{h,k}$ and breathing $r_{b,k}$ when compensation starts. 3) The compensation voltage and the ECG signal.

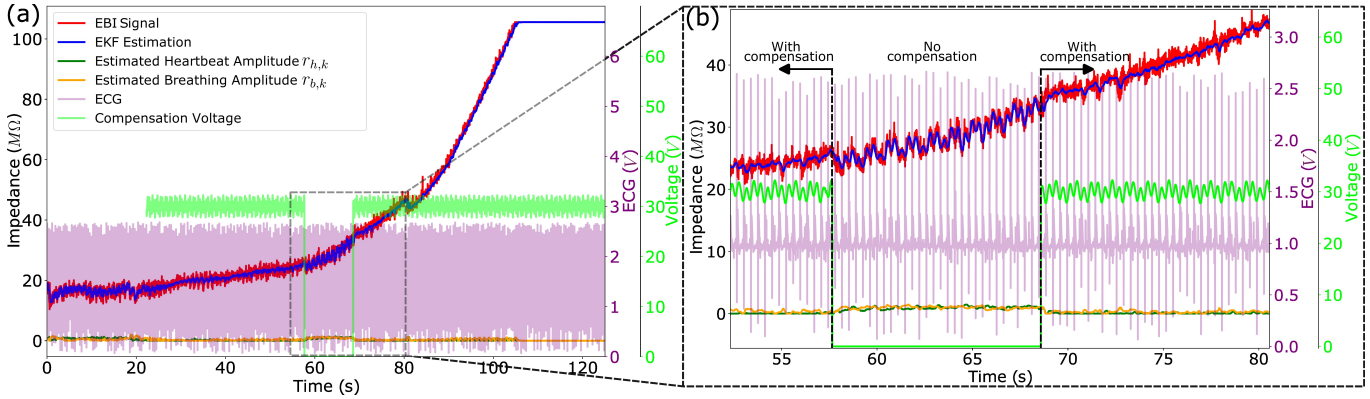

Fig. 11. *In vivo* motion compensation during forward advancement while also making contact with the object under test. (a) The whole procedure of the experiment with the patch point. (b) The difference of the EBI, estimated amplitude between with and without motion compensation.

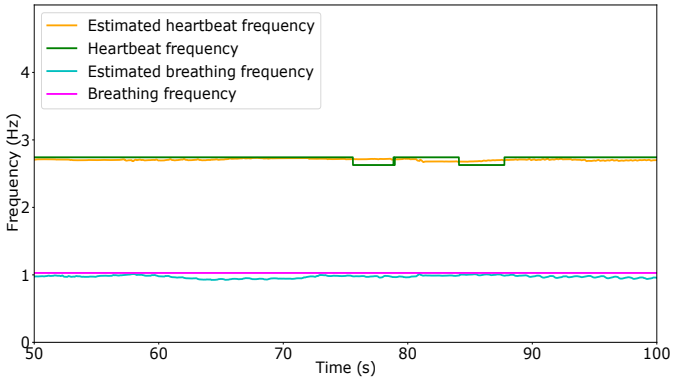

Fig. 12. Frequencies of both heartbeat and breathing during the *in vivo* patch clamp.

the pipette toward the neuron. According to the impedance-distance relationship described in Sec. II-B, the impedance will increase as it approaches the neuron. In the extreme the impedance (resistance) will grow to infinity, in our realistic application this means clipping the value. This is illustrated in Fig. 11(a) where this kind of progression from enabling compensation ($\sim$ 25 s) until clipping ($\sim$ 100 s; end of forward movement) is shown. Note that for a certain period of time ($\sim$ 58 - 68 s) the compensation was temporarily disabled. Details of this period are in panel (b), where the fluctuations induced by the physiological motion appear again on the EBI when there is no motion compensation. The estimated amplitudes for both heartbeat and respiratory motion (i.e., $r_{h,k}$ and $r_{b,k}$) components also increased after the algorithm was manually stopped. When the algorithm was started again, the fluctuations of the EBI signal were minimized and both amplitudes estimated by the EKF decreased, which indicates the relative motion between the tip of the pipette and the neuron membrane is reduced. This example illustrates the algorithm's ability to maintain compensation in the presence of a dynamically changing operating point.

To further demonstrate the performance of the proposed control strategy, Fig. 12 shows the estimated frequencies of both heartbeat and breathing from the EKF between 50 s - 100 s during the *in vivo* patch clamp procedure. The heartbeat and breathing frequencies of the animal were calculated through the Fast Fourier Transform (FFT) with a window of 500 data points, which for a sample rate of 100 Hz in this work, leads to a 5 s time window. It is clear to observe that with motion compensation and pipette approaching neurons, the proposed controller can still perform stable and maintains an accurate estimation of physiological motion frequencies.

Reaching the motion compensation during the *in vivo* experiment shows the promising performance of the proposed algorithm. It provides great potential for further patch clamp since this approach procedure is the essential step when performing the in vivo patch clamp on the neurons.

V. Discussion

The aim of this work was to develop a mechanical setup and EKF algorithm to compensate for the physiological motion of a neuron to ease the procedure of *in vivo* patch clamp experiments.

In this work, a motion compensation strategy solely based on EBI sensing, using the available patch pipette is proposed. For this, we exploited the monotonically decreasing impedance-distance trend between pipette and object (Parafilm®) as was characterized in our previous work using *ex vivo* calf brain [45]. The difference in the impedance-distance relationship (between different test objects or between benchtop and *in vivo* setup) is not a barrier in this work. Moreover, it is not advisable to depend on it since pulled pipettes can vary significantly in impedance. Furthermore, due to temperature, stress level, and accessibility, the environment itself will also vary under *in vivo* experiment conditions. Thus, the proposed method is designed to be independent of specific pipettes and environmental characteristics. An attention point in the impedance-distance relationships in Fig. 2(b) is saturation due to practical limitations (e.g., voltage clipping in EBI sensor, current leakage between pipette and object, etc.). This saturation is unavoidable and can be mitigated by choosing another (larger) operating range, which in turn results in a lower signal-to-noise ratio at large distances. During development on the test bench, we used a fixed range, and in the in vivo setup, the range was chosen based on the intended purpose (i.e., distal or proximal compensation).

To develop and verify the proposed motion compensation strategy, an experimental benchtop setup was built with motion sensors and simulation capabilities. Two different observation models were tested, a simple for only a dominant heartbeat and an advanced one for both heartbeat and breathing. Different scenarios over a range of heartbeat frequencies were tested. Results showed that over different conditions the CPs were larger than 73% for the simple model and larger than 81% for the advanced model, which is reasonable because one more component (breathing) is included in the observation model despite it not being the major source of the physiological motion compared to the heartbeat. This also shows the potential of the algorithm for the following *in vivo* experiment, here solely based on the bio-impedance measurement, and illustrates the stability of the benchtop setup.

For *in vivo* experiments, a lean-and-mean setup using the advanced model was developed, where a compensation result of at least 75% was achieved. The *in vivo* performance is very good, but as expected less than on that of the benchtop. This is for instance due to differences in environment (*in vivo* brain versus saline water in a cup), stimulus (i.e., the discrepancy between model and reality, dynamic behavior such as rate changes), setup (e.g. different pipette, less mechanical stability), and scenarios (static vs. dynamic behavior). During and after a successful patch, the EBI will reach saturation and lose its function (shown in Fig. 11(a) after $\sim$ 110 s). It is up to the experimenter whether or not to turn off motion compensation. The result of the latter is unpredictable due to loss of feedback and is not recommended. In most cases, after a successful patch, it is even not necessary anymore given the flexibility of the neuron.

Due to the space limitations of the patch pipette (shown in Fig. 9), only one EBI sensor was implemented here. Based on this, the motion compensation control strategy was proposed in Sec. II-D. The amplitude will stop updating when the variation is lower than a preset threshold value, which now the measured bioimpedance signal is close to a flat line and indicates no relative motion between the pipette tip and the neuron surface. The lower the threshold value, the less residual motion will remain and the measured EBI signal will be closer to a flat line. However, a smaller threshold value will also compromise the measured EBI signal since it contains less information about the motion. Nevertheless, the closer to the neurons, the less fluctuation of the impedance range when distance changes (Fig. 2). Thus, the performance of the system will not be influenced too much by choosing different preset thresholds, which shows the robust stability of the proposed control strategy. Furthermore, the combination of the EKF and the EBI provides a novel way of detecting the motion of the neurons and using it for motion compensation.

For future study, other biological signals that may link to the physiological motion (e.g. ECG) are suggested to be implemented with the EBI together to provide a more accurate and stable motion detection source. Moreover, a more advanced control schematic with other signal inputs is also considered to be integrated with the current system.

VI. Conclusion

In this work, an EKF-based motion compensation strategy to neutralize the motion of a neuron by using only EBI sensing is proposed. Measurements obtained under different conditions and scenarios showed a compensation performance of at least 80% and 75% for the benchtop and *in vivo* setup, respectively. The capabilities of the current technique have been successfully demonstrated, which has the great potential to significantly improve the success rate of *in vivo* intracellular experiments and other related applications.

References

[1] E. Verschooten *et al.*, "Auditory nerve frequency tuning measured with forward-masked compound action potentials," *J. of the Assoc. for Res. in Otolaryngology*, vol. 13, no. 6, pp. 799–817, 2012.

[2] C. Bargmann *et al.*, "Brain 2025: a scientific vision," *Brain Research through Advancing Innovative Neurotechnologies (BRAIN) Working Group Report 06052014 to the Advisory Committee to the Director, NIH*, 2014.

[3] R. Brette and A. Destexhe, "Intracellular recording," *Handbook of neural activity measurement*, pp. 44–91, Cambridge University Press, Cambridge, UK, 2012.

[4] B. G. Kornreich, "The patch clamp technique: principles and technical considerations," *Journal of Veterinary Cardiology*, vol. 9, no. 1, pp. 25–37, 2007.

[5] W. Gerstner and W. M. Kistler, *Spiking neuron models: Single neurons, populations, plasticity*. Cambridge university press, 2002.

[6] E. Neher and B. Sakmann, "The patch clamp technique," *Scientific American*, vol. 266, no. 3, pp. 44–51, 1992.

[7] M. Yoshimura and S. Nishi, "Blind patch-clamp recordings from substantia gelatinosa neurons in adult rat spinal cord slices: pharmacological properties of synaptic currents," *Neuroscience*, vol. 53, no. 2, pp. 519–526, 1993.

[8] J. Gorelik *et al.*, "Ion channels in small cells and subcellular structures can be studied with a smart patch-clamp system," *Biophysical journal*, vol. 83, no. 6, pp. 3296–3303, 2002.

[9] T. W. Margrie, M. Brecht, and B. Sakmann, "In vivo, low-resistance, whole-cell recordings from neurons in the anaesthetized and awake mammalian brain," *Pflügers Archiv*, vol. 444, no. 4, pp. 491–498, 2002.

[10] J. Muthuswamy *et al.*, "Electrostatic microactuators for precise positioning of neural microelectrodes," *IEEE Transactions on Biomedical Engineering*, vol. 52, no. 10, pp. 1748–1755, 2005.

[11] S. Lee *et al.*, "Motion characterization scheme to minimize motion artifacts in intravital microscopy," *Journal of Biomedical Optics*, vol. 22, no. 3, p. 036005, 2017.

[12] M. S. Fee, "Active stabilization of electrodes for intracellular recording in awake behaving animals," *Neuron*, vol. 27, no. 3, pp. 461–468, 2000.

[13] A. Gilletti and J. Muthuswamy, "Brain micromotion around implants in the rodent somatosensory cortex," *Journal of Neural Engineering*, vol. 3, no. 3, p. 189, 2006.

[14] N. Sharafkhani *et al.*, "Neural tissue-microelectrode interaction: Brain micromotion, electrical impedance, and flexible microelectrode insertion," *Journal of Neuroscience Methods*, vol. 365, p. 109388, 2022.

[15] W. M. Stoy *et al.*, "Compensation of physiological motion enables high-yield whole-cell recording in vivo," *Journal of Neuroscience Methods*, vol. 348, p. 109008, 2021.

[16] A. K. Lee *et al.*, "Head-anchored whole-cell recordings in freely moving rats," *Nature protocols*, vol. 4, no. 3, pp. 385–392, 2009.

[17] S. B. Kodandaramaiah *et al.*, "Automated whole-cell patch-clamp electrophysiology of neurons in vivo," *Nature methods*, vol. 9, no. 6, pp. 585–587, 2012.

[18] S. Lee *et al.*, "Image stabilization for in vivo microscopy by high-speed visual feedback control," *IEEE Transactions on Robotics*, vol. 24, no. 1, pp. 45–54, 2008.

[19] K. Kitamura *et al.*, "Targeted patch-clamp recordings and single-cell electroporation of unlabeled neurons in vivo," *Nature methods*, vol. 5, no. 1, pp. 61–67, 2008.

[20] H.-J. Suk *et al.*, "Image-guided closed-loop robotic system for automated whole-cell patch clamping electrophysiology of neurons in vivo," May 4 2021, US Patent 10,993,634.

[21] M. J. Musa *et al.*, "Respiratory compensated robot for liver cancer treatment: Design, fabrication, and benchtop characterization," *IEEE/ASME Transactions on Mechatronics*, vol. 27, 2022.

[22] L. Cheng and M. Tavakoli, "Ultrasound image guidance and robot impedance control for beating-heart surgery," *Control Engineering Practice*, vol. 81, pp. 9–17, 2018.

[23] R. Cabrera-Lozoya *et al.*, "Image-based biophysical simulation of intracardiac abnormal ventricular electrograms," *IEEE Transactions on Biomedical Engineering*, vol. 64, no. 7, pp. 1446–1454, 2016.

[24] O. Al-Ahmad *et al.*, "Local one-dimensional motion estimation using FBG-based shape sensing for cardiac applications," *IEEE Robotics and Automation Letters*, vol. 7, no. 3, pp. 8122–8129, 2022.

[25] T. Koivumäki *et al.*, "An integrated bioimpedance—ECG gating technique for respiratory and cardiac motion compensation in cardiac PET," *Physics in Medicine & Biology*, vol. 59, no. 21, p. 6373, 2014.

[26] L. Cheng and M. Tavakoli, "Neural network-based physiological organ motion prediction and robot impedance control for teleoperated beating-heart surgery," *Biomedical Signal Processing and Control*, vol. 66, 2021.

[27] Z. Jiang *et al.*, "Precise repositioning of robotic ultrasound: Improving registration-based motion compensation using ultrasound confidence optimization," *IEEE Transactions on Instrumentation and Measurement*, vol. 71, pp. 1–11, 2022.

[28] D. Wu *et al.*, "Hysteresis modeling of robotic catheters based on long short-term memory network for improved environment reconstruction," *IEEE Robot. and Automat. Lett.*, vol. 6, no. 2, pp. 2106–2113, 2021.

[29] P. Kassanos, "Bioimpedance sensors: A tutorial," *IEEE Sensors Journal*, vol. 21, no. 20, pp. 22 190–22 219, 2021.

[30] M. Guermazi *et al.*, "Investigation of long time beef and veal meat behavior by bioimpedance spectroscopy for meat monitoring," *IEEE Sensors Journal*, vol. 14, no. 10, pp. 3624–3630, 2014.

[31] Z. Cheng *et al.*, "An electrical bioimpedance scanning system for subsurface tissue detection in robot assisted minimally invasive surgery," *IEEE Trans. on Biomed. Eng.*, vol. 69, no. 1, pp. 209–219, 2021.

[32] L. Schoevaerdts *et al.*, "Design and evaluation of a new bioelectrical impedance sensor for micro-surgery: application to retinal vein cannulation," *International Journal of Computer Assisted Radiology and Surgery*, vol. 14, no. 2, pp. 311–320, 2019.

[33] L. Schoevaerdts *et al.*, "Electrical bio-impedance proximity sensing for vitreo-retinal micro-surgery," *IEEE Robotics and Automation Letters*, vol. 4, no. 4, pp. 4086–4093, 2019.

[34] R. J. Halter and Y.-J. Kim, "Toward microendoscopic electrical impedance tomography for intraoperative surgical margin assessment," *IEEE Trans. on Biomed. Eng.*, vol. 61, no. 11, pp. 2779–2786, 2014.

[35] Z. Cheng *et al.*, "Smartprobe: a bioimpedance sensing system for head and neck cancer tissue detection," *Physiological measurement*, vol. 41, no. 5, p. 054003, 2020.

[36] Z. Cheng *et al.*, "Active search of subsurface lymph nodes using robot-assisted electrical impedance scanning," *IEEE Transactions on Instrumentation and Measurement*, vol. 71, pp. 1–11, 2022.

[37] R. Kusche and M. Ryschka, "Combining bioimpedance and EMG measurements for reliable muscle contraction detection," *IEEE Sensors Journal*, vol. 19, no. 23, pp. 11 687–11 696, 2019.

[38] R. J. Meinhold and N. D. Singpurwalla, "Understanding the kalman filter," *The American Statistician*, vol. 37, no. 2, pp. 123–127, 1983.

[39] T. Lefebvre, H. Bruyninckx, and J. De Schutter, "Kalman filters for non-linear systems: a comparison of performance," *International journal of Control*, vol. 77, no. 7, pp. 639–653, 2004.

[40] R. J. Elliott, L. Aggoun, and J. B. Moore, *Hidden Markov models: estimation and control*. Springer Science & Business Media, Berlin, Germany, 2008, vol. 29.

[41] K. Youngjoo and B. Hyochoong, "Introduction to kalman filter and its applications," *Intechopen, London*, 2018.

[42] S. G. Yuen *et al.*, "Force tracking with feed-forward motion estimation for beating heart surgery," *IEEE Transactions on Robotics*, vol. 26, no. 5, pp. 888–896, 2010.

[43] O. Al-Ahmad *et al.*, "Force control with a novel robotic catheterization system based on braided sleeve grippers," *IEEE Transactions on Medical Robotics and Bionics*, pp. 1–1, 2023.

[44] P. Flecknell, "Anaesthesia of animals for biomedical research," *BJA: British Journal of Anaesthesia*, vol. 71, no. 6, pp. 885–894, 1993.

[45] K. Van Assche *et al.*, "Physiological motion compensation in patch clamping using electrical bio-impedance sensing," in *2023 International Symposium on Medical Robotics (ISMR)*. IEEE, 2023, pp. 1–7.



Yao Zhang received the M.Sc. degree in medical technology and engineering from the Technical University of Munich, Munich, Germany in 2021. He is currently working toward the Ph.D. degree with Katholieke Universiteit Leuven, Leuven, Belgium, under the Fonds Wetenschappelijk Onderzoek (FWO) fellowship.

He received the Honorable Mentions of the Best Paper Award of *IEEE Robotics and Automation Letters (RA-L)* in 2021. He also received the Best Student Paper Award at the *IEEE International Symposium on Medical Robotics* in 2023.



Eric Verschooten received two M.S. degrees in electrical engineering from University of Leuven, Belgium, in 1995 and 1998, and a Ph.D. degree in biomedical sciences from the same university in 2013. Since 2013, he has been a postdoctoral researcher in the laboratory of Auditory Neurophysiology, Department of Neuroscience, University of Leuven, Belgium. From 2006-2007, he was a visiting professor at the Faculty of Applied Sciences University of Antwerp, Belgium. From 2000-2006, he was consultant in electronic engineering, high-end TVs, and LED applications, at Philips, Brugges, Belgium, and Eindhoven, The Netherlands. From 1998-2000, he was a semiconductor research engineer at the Interuniversity Microelectronics Centre, Leuven, Belgium.



Mouloud Ourak received the M.S. degree in robotics and vision from the Université de Montpellier, Montpellier, France, in 2013, and the Ph.D. degree in automation from the Université de Franche-Comté, Besançon, France, in 2016.

Since 2017, he has been a Postdoctoral Researcher with the Robot-Assisted Surgery Group, Department of Mechanical Engineering, Katholieke Universiteit Leuven, Leuven, Belgium. His research interests include surgical microrobotics (actuators and control laws) and visual servoing.



Kaat Van Assche received the M.Sc. degree in electromechanical engineering, with a specialization in clinical engineering from KU Leuven University, Belgium, in 2022. She is currently pursuing the Ph.D. degree with the Robot-Assisted Surgery (RAS) group at KU Leuven. Her first-authored article was awarded the Best Student Paper Award at the *IEEE International Symposium on Medical Robotics* in 2023. Her research interests include medical robotics, medical image processing and deep learning.



Gianni Borghesan received the M.S. degree in information engineering from the University of Pisa, Pisa, Italy, in 2004, and the Ph.D. degree in automation and operative research from the University of Bologna, Bologna, Italy, in 2008.

From 2008 to 2010, he was a Postdoctoral Researcher with the University of Bologna. Since 2010, he has been with the Department of Mechanical Engineering, Katholieke Universiteit Leuven, Leuven, Belgium, participating in several research projects in the field of robotics. He is currently a Research Expert with the Department of Mechanical Engineering and Core Lab ROB, Flanders Make, Katholieke Universiteit Leuven. His research interests include constraint-based control, teleoperation and haptics, and robotic surgery.



Di Wu received the M.Sc. degree in medical technology and engineering, from the Technical University of Munich (TUM), Germany, in 2019. He is currently working toward a double Ph.D. degree at KU Leuven, Belgium, and the Delft University of Technology, Netherlands, under the Marie Skáodowska-Curie Actions of the European Union Horizon 2020. From 2018 to 2019, he was a Visiting Graduate Researcher at the Johns Hopkins University, USA. In 2023, he was a visiting PhD student at The BioRobotics Institute of Scuola Superiore Sant'Anna, Pisa, Italy.

His first-authored paper received an Honorable Mention for the Best Paper Award from *IEEE Robotics and Automation Letters (RA-L)* in 2021, and another was a finalist for the Best Paper Award at the *IEEE International Symposium on Medical Robotics (ISMR)* in 2019. He also received travel grants/awards from *IEEE/RSJ International Conference on Intelligent Robots and Systems (IROS)* 2022, *IEEE International Conference on Robotics and Automation (ICRA)* 2023, and Fonds Wetenschappelijk Onderzoek (FWO).

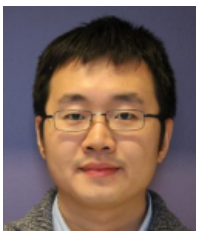

Kenan Niu received BSc and MSc degrees in Biomedical Engineering, with honors (Cum Laude), from Northeastern University (China) in 2011 and 2013, respectively. During his studies, he specialized in medical image processing and surgical navigation. In 2018, Dr. Niu obtained his doctoral degree in Biomechanical Engineering from the University of Twente. After PhD, Dr. Niu worked as a postdoctoral researcher at imec-Vision Lab at the University of Antwerp (2019) and in the Robot-assisted Surgery group (2020-2022) at KU Leuven (Belgium). Currently, he serves as an Assistant Professor in the Robotics and Mechatronics (RAM) Group at the University of Twente (the Netherlands) since May 2022. His research interests encompass various areas, including robotic imaging, robotic orthopedic surgery, robotic ultrasound imaging, surgical navigation, and AR/VR.



Philip X. Joris joined the University of Leuven in 1995 as a Professor in the Department of Neuroscience. He received MD and PhD degrees from the University of Antwerp (Belgium) in 1983 and 1992, respectively. He did postdoctoral work at UCSF and U.W.-Madison. He researches cochlear and brainstem mechanisms of hearing, with a focus on small circuits involved in temporal processing toward pitch and sound localization. These circuits are studied with axonal, whole-cell, and extracellular recording techniques and structure-function techniques in a variety of animal models. Combination with mass potential recordings in animals and humans extends the relevance of the findings toward the understanding of human hearing



Emmanuel Vander Poorten received the M.S. degree in mechanical engineering from KU Leuven, Leuven, Belgium, in 2001, and the Ph.D. degree in mechanical engineering from Kyoto University, Kyoto, Japan, in 2007.

He is currently an Associate Professor with the Department of Mechanical Engineering, Katholieke Universiteit Leuven, Leuven, Belgium. He is the Coordinator of the Robot-Assisted Surgery Group, the Founder of *Conference on New Technologies for Computer and Robot Assisted Surgery (CRAS)*, the Joint Conference on New Technologies for Computer/Robot-Assisted Surgery, and a Steering Board Member of ACTUATOR a biennial event bringing together leading experts, suppliers, and users of new actuators and low-power electromagnetic drives. He is active in international collaborative research projects, participating, and coordinating several European Union-funded projects on medical robotics. His research interests include medical device design, robotic co-manipulation, haptics, teleoperation, control of flexible instruments, and robotic catheters